Science Advances
AAAS

advances.sciencemag.org/cgi/content/full/6/10/eaaz3112/DC1

Supplementary Materials for

An ultrastable lithium metal anode enabled by designed metal fluoride spansules

Huadong Yuan, Jianwei Nai, He Tian, Zhijin Ju, Wenkui Zhang, Yujing Liu, Xinyong Tao*, Xiong Wen (David) Lou*

*Corresponding author. Email: tao@zjut.edu.cn (X.T.); xwlou@ntu.edu.sg (X.W.L.)

Published 6 March 2020, *Sci. Adv.* **6**, eaaz3112 (2020)
DOI: 10.1126/sciadv.aaz3112

This PDF file includes:

Fig. S1. FESEM images of the Li plated on bare Cu foil.
Fig. S2. FESEM images of the Li plated on the NMMF@C-Cu with the capacity of 0.5 mAh cm^{-2} at the current density of 0.5 mA cm^{-2}.
Fig. S3. FESEM images of the Li plated on the NMMF-Cu.
Fig. S4. Characterizations of the NMMF@C cubes after soaking in the ether electrolyte (DOL/DME) for 48 hours.
Fig. S5. XRD patterns of the NMMF@C before and after soaking in the ether electrolyte.
Fig. S6. Characterizations of the NMMF cubes after soaking in the ether electrolyte for 48 hours.
Fig. S7. ICP-MS results showing the concentration of various metal ions in the ether electrolyte for the same period.
Fig. S8. The dissolution behavior of NMMF@C as a function of time in the ether electrolyte.
Fig. S9. The initial discharge curve of the NMMF@C-Cu anode during the activation process at the current density of 50 mA g^{-1}.
Fig. S10. FESEM and elemental mapping images of Li plating on b-Cu with several NMMF@C particles.
Fig. S11. A depth profiling of the elements on the Li-plated NMMF@C sample with a capacity of 0.5 mAh cm^{-2} by XPS sputter etching technique.
Fig. S12. A cryo-TEM image of the Li deposited on the NMMF@C-modified Cu grid.
Fig. S13. Cryo-TEM characterization for the M layer.
Fig. S14. XPS characterization.
Fig. S15. EDX characterization.
Fig. S16. Electrochemical Li plating curves on NMMF@C-Cu anodes at 1 mA cm^{-2} for 1 mAh cm^{-2} during the 100th, 200th, 300th, 400th, and 500th cycles.
Fig. S17. The CE versus cycle number plot of the LMA on b-Cu using NaF as the electrolyte additive.
Fig. S18. The cycle life of the NMMF@C-Cu electrode at the current densities of 1 and 2 mA cm^{-2}.
Fig. S19. Morphology and electrochemical performance of the Cu electrodes with different loading thickness of NMMF@C.

Fig. S20. The CE of Li deposition/stripping on the NMMF@C-Cu electrode at high areal capacities.
Fig. S21. Nucleation overpotential and polarization potential.
Fig. S22. The EIS plots of the NMMF@C-Cu and b-Cu electrodes after the 1st and 50th cycles.
Fig. S23. Arrhenius plot of the symmetric NMMF@C-Li//NMMF@C-Li cell.
Fig. S24. EIS plots of the symmetric cell at 1 mA cm^{-2} for 1 mAh cm^{-2}.
Fig. S25. The first charge curves of three NCM811/NMMF@C-Li full cells at the current density of 100 mA g^{-1}.
Fig. S26. FESEM images of the plated Li and separator in a symmetric cell after 400 cycles.
Fig. S27. Charge/discharge curves of full cells.
Fig. S28. Rate capability of the NCM811/Cu-Li full cell.
Table S1. The mass loss of NMMF@C in the ether electrolyte as a function of time.
Table S2. The comparison of the CE of the anode in our work and some reported state-of-the-art anodes tested in the DOL/DME ether electrolyte.
References (*53–57*)

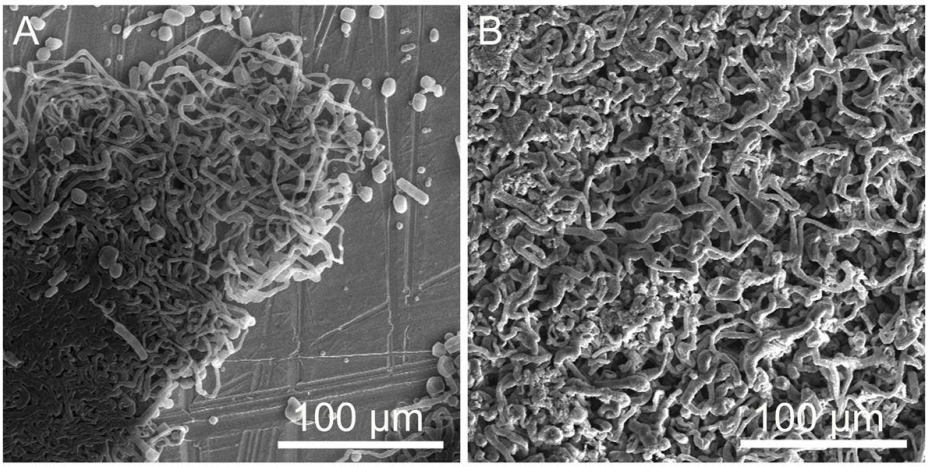

Fig. S1. FESEM images of the Li plated on bare Cu foil. The deposited capacities of Li metal are (**A**) 0.5 and (**B**) 2 mAh cm^{-2} at the current density of 0.5 mA cm^{-2}.

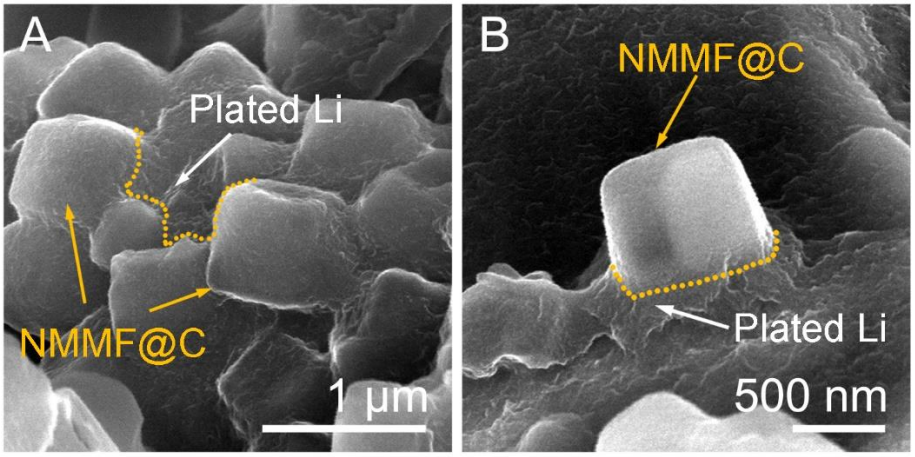

Fig. S2. FESEM images of the Li plated on the NMMF@C-Cu with the capacity of 0.5 mAh cm^{-2} at the current density of 0.5 mA cm^{-2}. (**A** and **B**) FESEM images of the regions showing the interface of the NMMF@C cubes and plated Li.

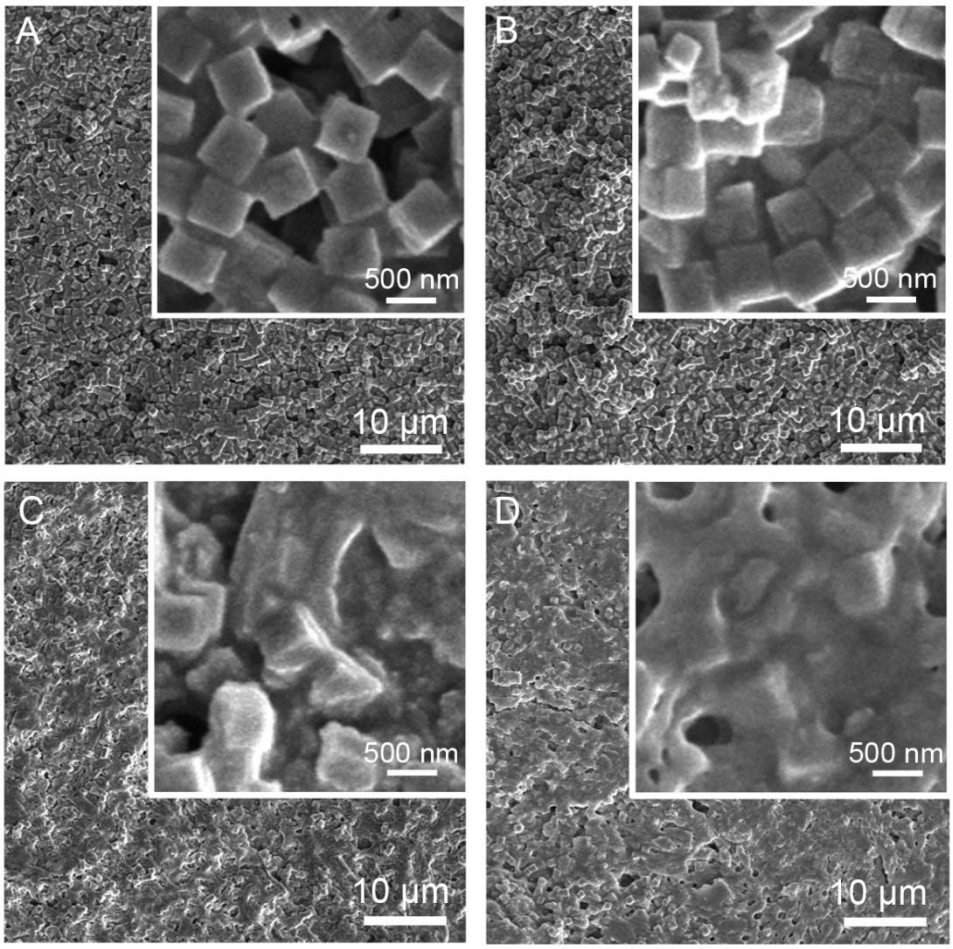

Fig. S3. FESEM images of the Li plated on the NMMF-Cu. The plated Li metal capacities are (**A**) 0.2, (**B**) 0.5, (**C**) 1, and (**D**) 2 mAh cm^{-2} at the current density of 0.5 mA cm^{-2}. These images show that Li was uniformly deposited on the NMMF-Cu, which is similar to that on the NMMF@C-Cu.

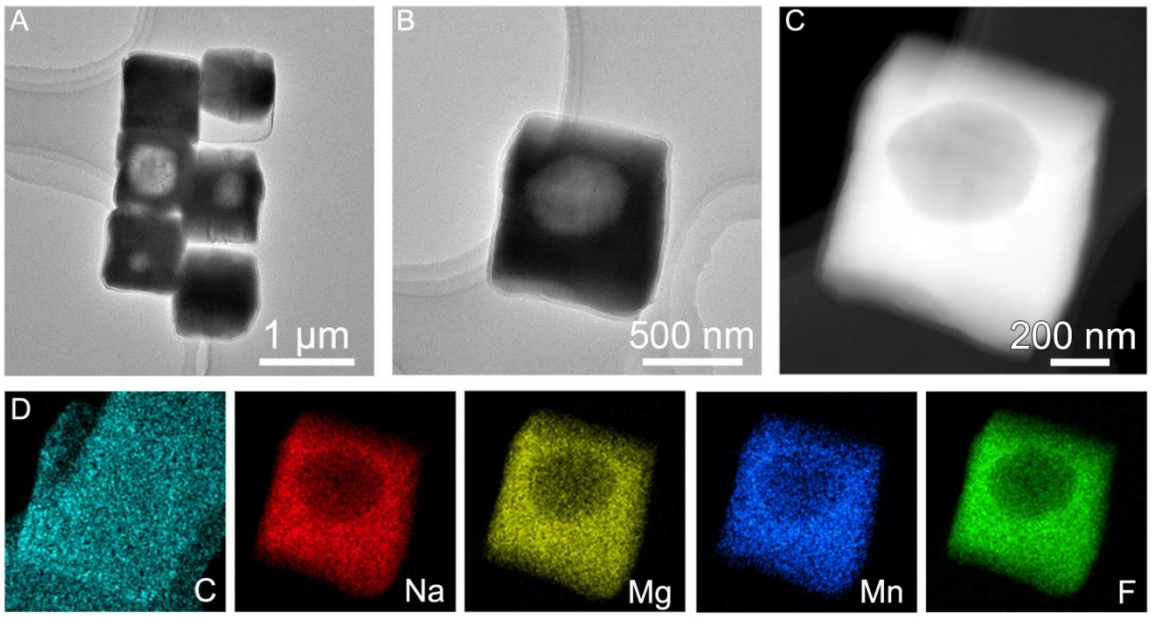

Fig. S4. Characterizations of the NMMF@C cubes after soaking in the ether electrolyte (DOL/DME) for 48 hours. (**A** and **B**) TEM images of the NMMF@C cubes. (**C**) STEM image and (**D**) related elemental mapping images of C, Na, Mg, Mn, and F. These data show that only a small part of the NMMF cubes is dissolved at this stage.

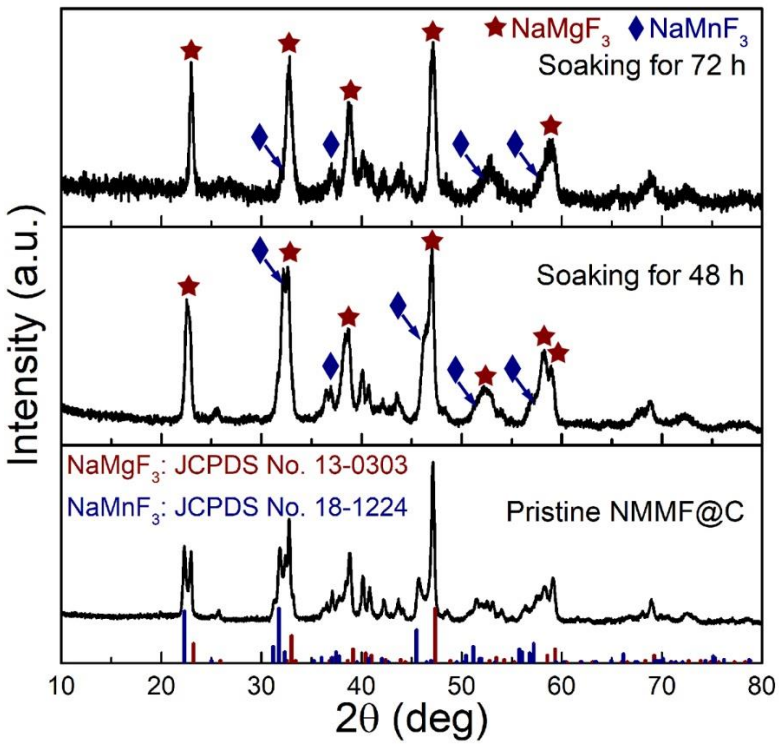

Fig. S5. XRD patterns of the NMMF@C before and after soaking in the ether electrolyte. The largely reduced intensity (from the absolute intensity data) of the XRD peaks for both the $NaMnF_3$ and $NaMgF_3$ phases indicates the dissolution of NMMF in the ether electrolyte.

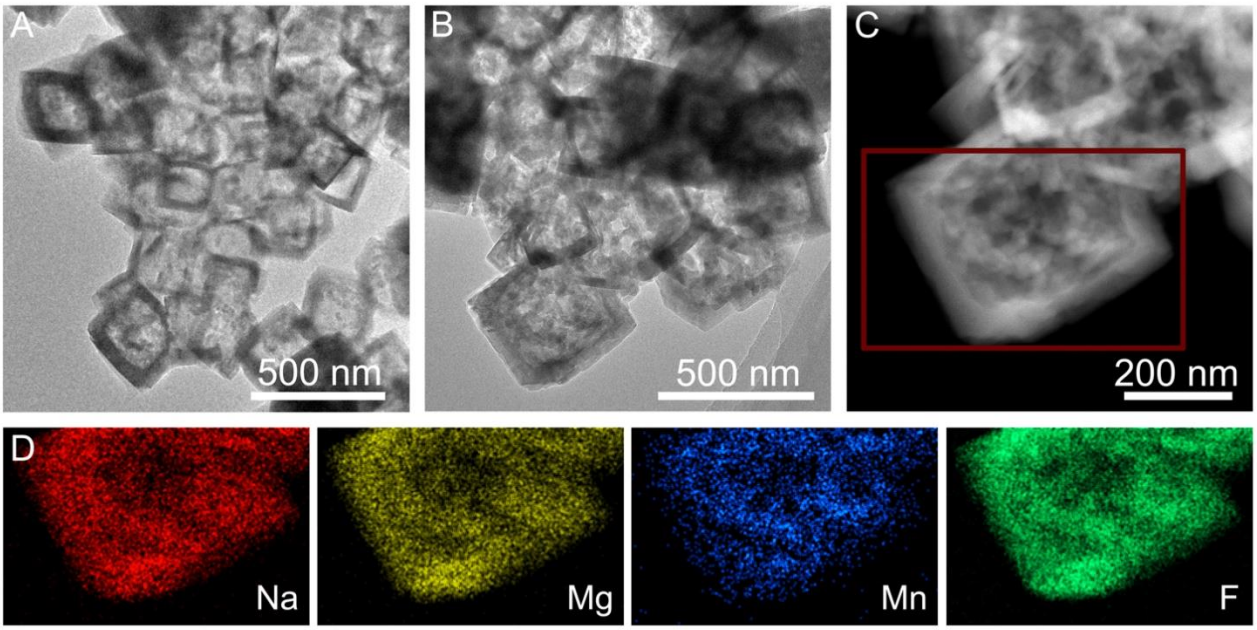

Fig. S6. Characterizations of the NMMF cubes after soaking in the ether electrolyte for 48 hours. (**A**-**C**) TEM images of the NMMF cubes. (**D**) The related elemental mapping images of Na, Mg, Mn, and F of the cube marked in (**C**). These data indicate that a large part of the NMMF cubes is dissolved at this stage.

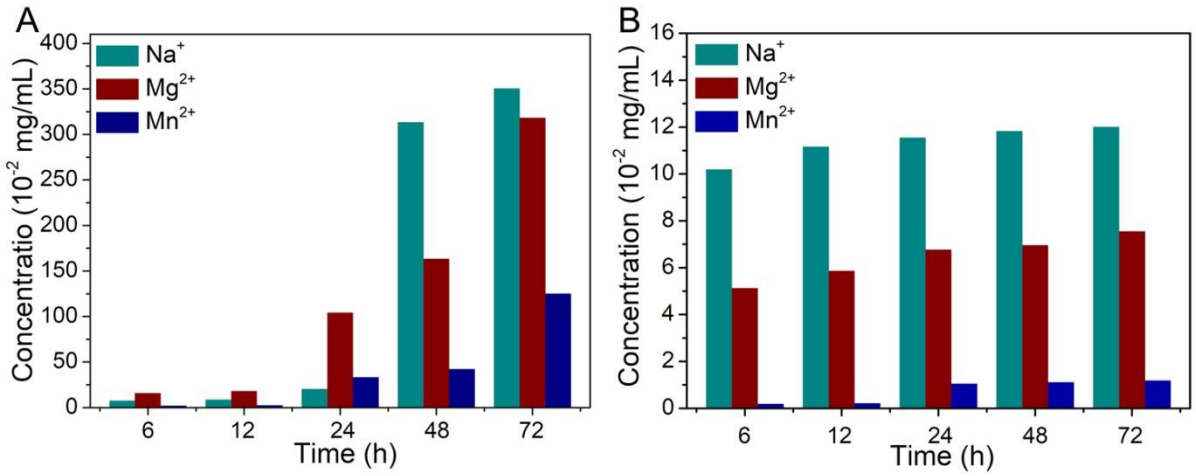

Fig. S7. ICP-MS results showing the concentration of various metal ions in the ether electrolyte for the same period. (**A**) The sample from the electrolyte containing NMMF. (**B**) The sample from the electrolyte containing NMMF@C.

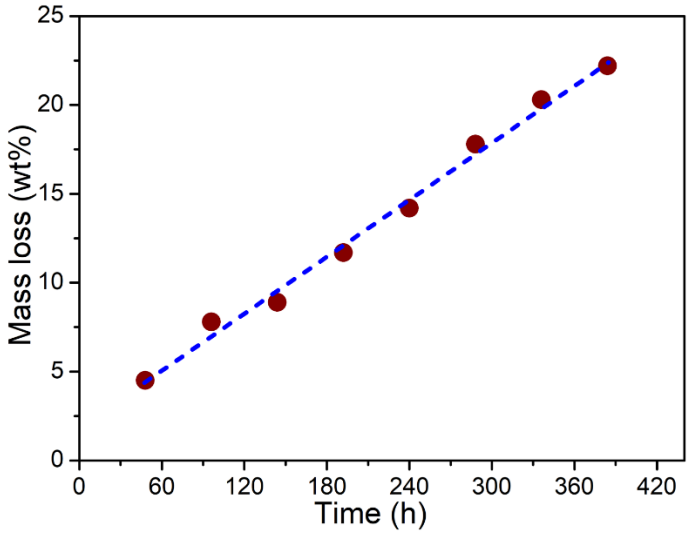

Fig. S8. The dissolution behavior of NMMF@C as a function of time in the ether electrolyte. This figure is plotted from the data in Table S1.

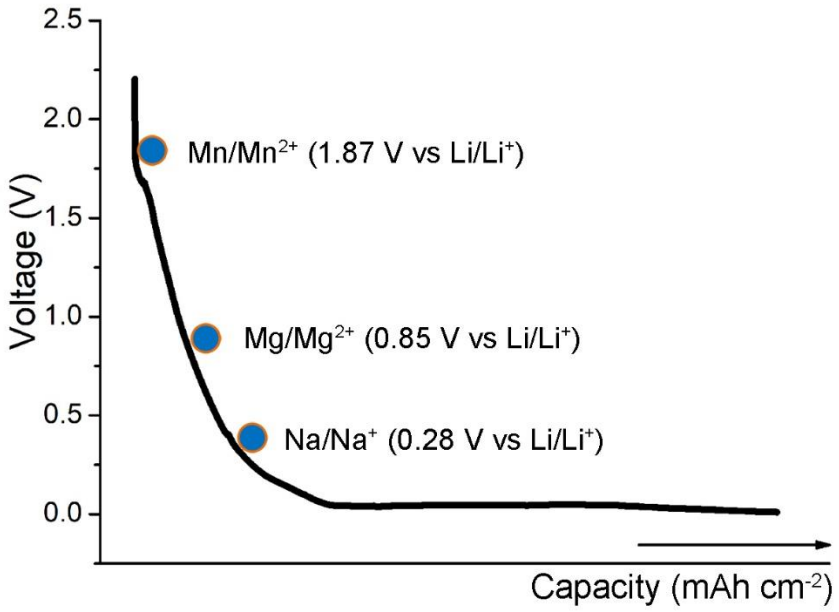

Fig. S9. The initial discharge curve of the NMMF@C-Cu anode during the activation process at the current density of 50 mA g^{-1}. Due to the higher redox potentials of Mn/Mn^{2+} (1.87 V *vs*. Li/Li^+), Mg/Mg^{2+} (0.85 V *vs*. Li/Li^+), and Na/Na^+ (0.28 V *vs*. Li/Li^+) than Li/Li^+, the dissolved metal ions (Na^+, Mg^{2+}, and Mn^{2+}) will be reduced on the matrix surface before the start of Li deposition.

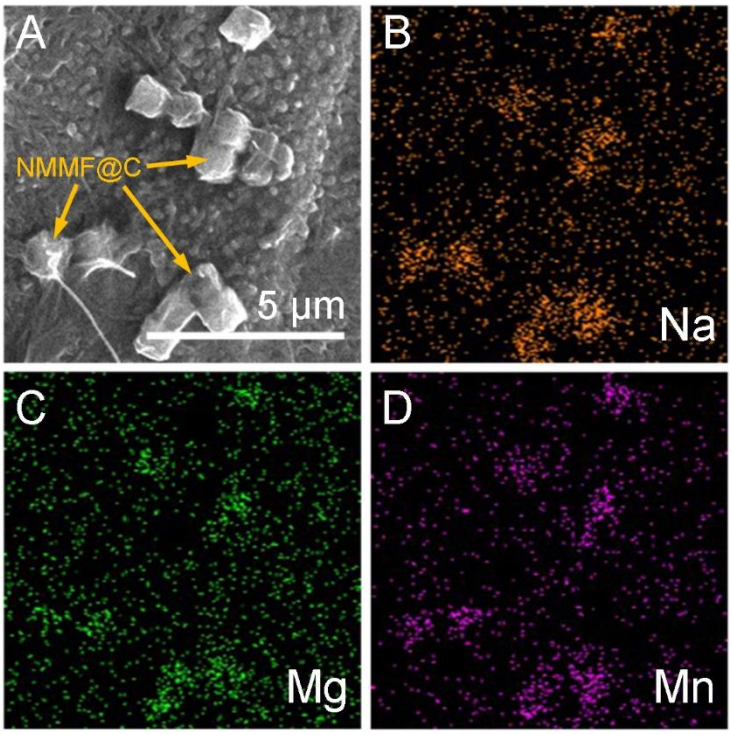

Fig. S10. FESEM and elemental mapping images of Li plating on b-Cu with several NMMF@C particles. (**A**) FESEM image of the sample, in which the NMMF@C particles are highlighted. (**B-D**) Corresponding elemental distribution of Na, Mg, and Mn. As can be seen, the deposited "M" is quite evenly distributed on the b-Cu regardless of NMMF@C particles, suggesting the formation of the M layer.

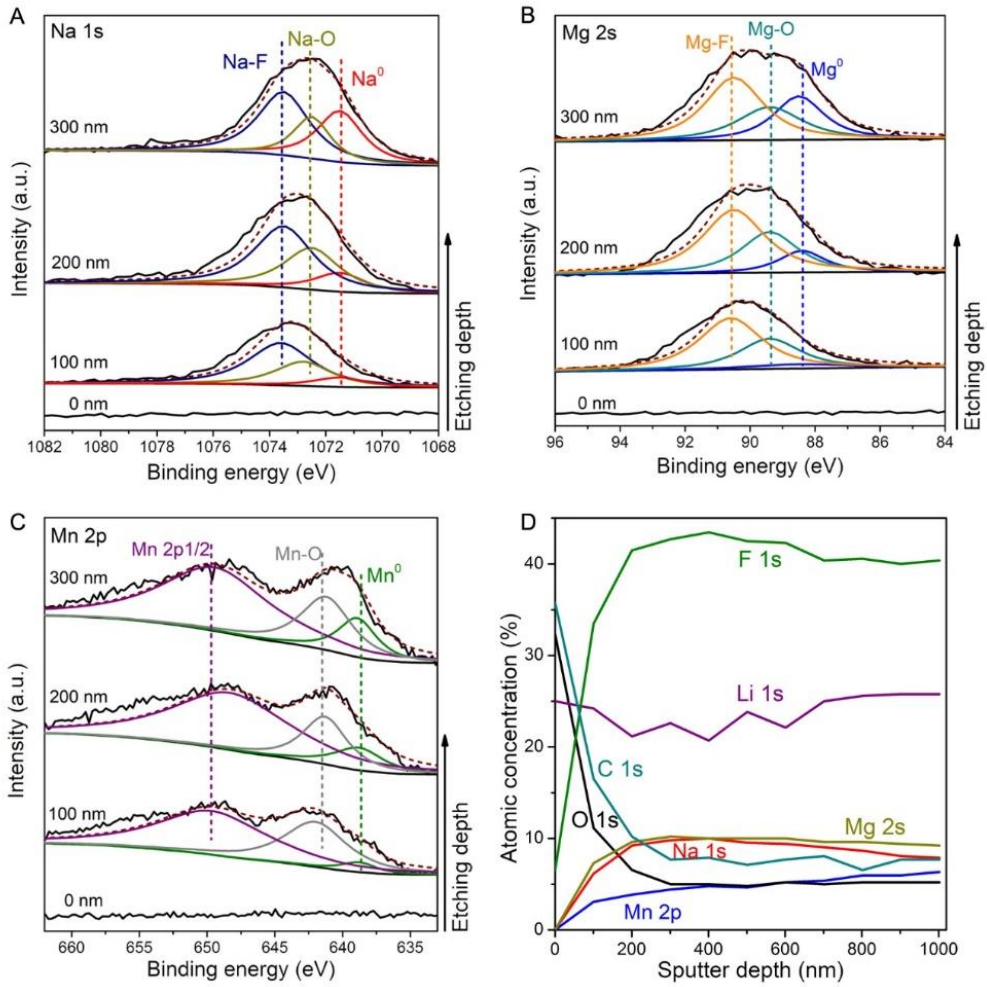

Fig. S11. A depth profiling of the elements on the Li-plated NMMF@C sample with a capacity of 0.5 mAh cm^{-2} by XPS sputter etching technique. (**A-C**) XPS spectra when the sputter etching was changed. (**D**) The elemental distribution with the function of the sputter depth. Results in fig. S11A-C confirm the presence of the metallic Na, Mg, and Mn, whose contents are all increased when the etching goes deeper. The elemental distributions shown in fig. S11D confirm our illustration proposed in Fig. 1 and Fig. 3G, and in agreement with the observation in Fig. 4F. For example, the O element originated from the Li_2O-based SEI is mainly located at the outer region. The F element should come from both the LiF-based SEI and the NMMF cubes. The Na, Mg, and Mn elements are mainly located at the inner region.

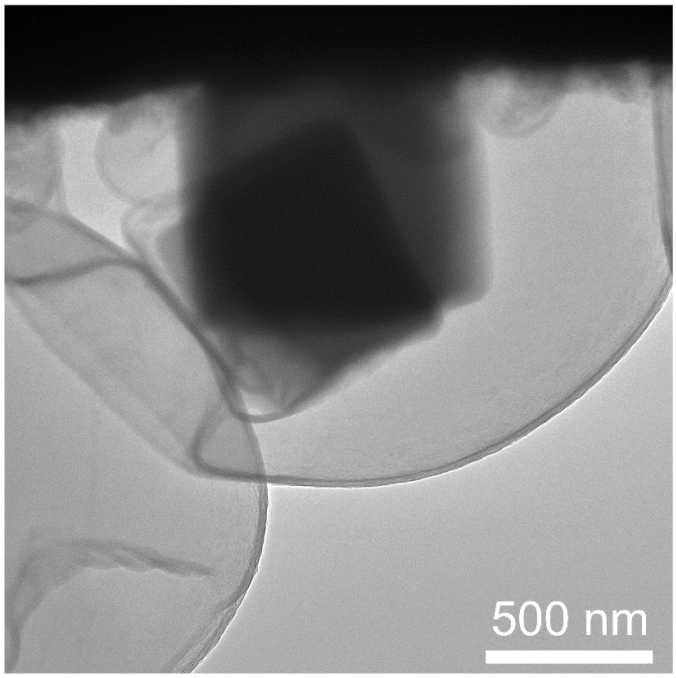

Fig. S12. A cryo-TEM image of the Li deposited on the NMMF@C-modified Cu grid. The plated Li capacity is 0.5 mAh cm^{-2} at the current density of 0.5 mA cm^{-2}.

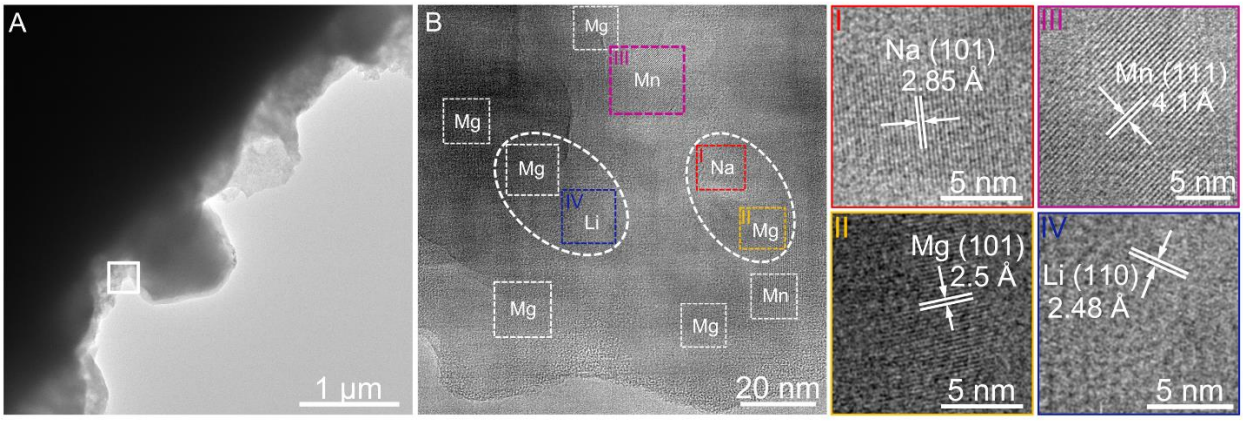

Fig. S13. Cryo-TEM characterization for the M layer. (**A**) Cryo-TEM image of the Li deposited on the NMMF@C modified Cu grid with the capacity of 0.2 mAh cm^{-2}. (**B**) A magnified TEM image of the Cu grid/NMMF@C interface region (marked with white rectangular) in fig. S13A. As revealed by related HRTEM images, metallic Na, Mg, and Mn nanograins can be found, indicating the formation of the M layer on the matrix surface.

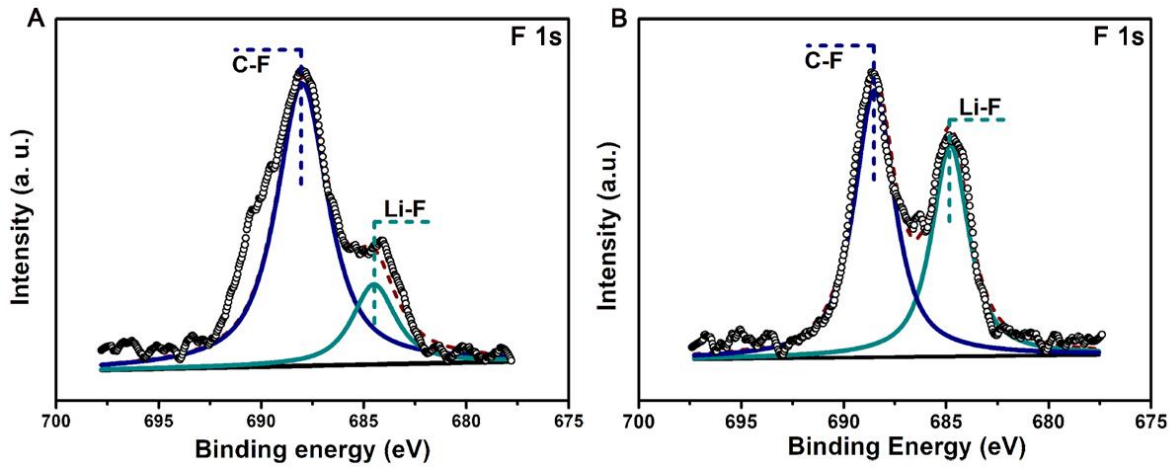

Fig. S14. XPS characterization. The F 1s spectra of the samples after the Li plating on (**A**) bare Cu grid and (**B**) NMMF@C modified Cu grid.

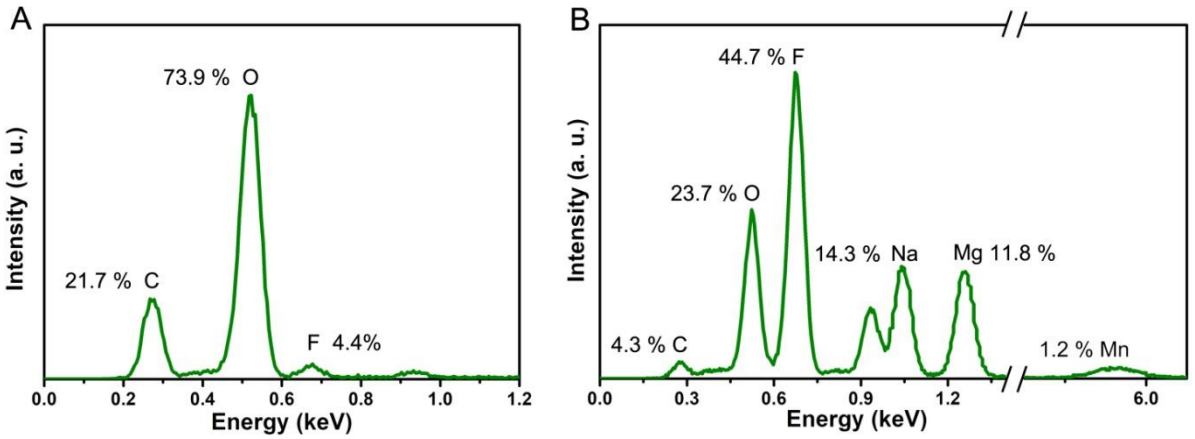

Fig. S15. EDX characterization. The element composition of samples after the Li plating on (**A**) bare Cu grid and (**B**) NMMF@C modified Cu grid.

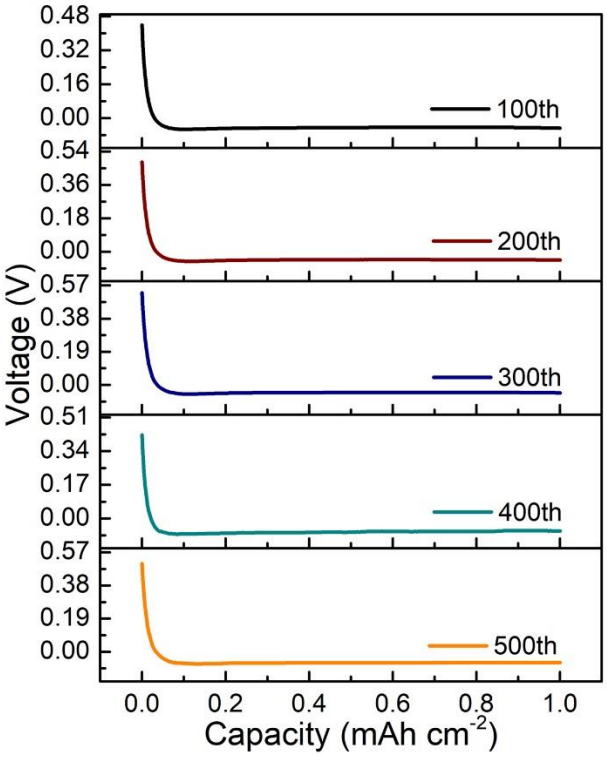

Fig. S16. Electrochemical Li plating curves on NMMF@C-Cu anodes at 1 mA cm^{-2} for 1 mAh cm^{-2} during the 100th, 200th, 300th, 400th, and 500th cycles. The absence of initial voltage "dip" (that is, almost zero overpotential) in these voltage curves suggests that the M-Li or C-Li alloying may be involved in the initial process of Li deposition (*Nat. Energy* **1**, 16010-16018 (2016)).

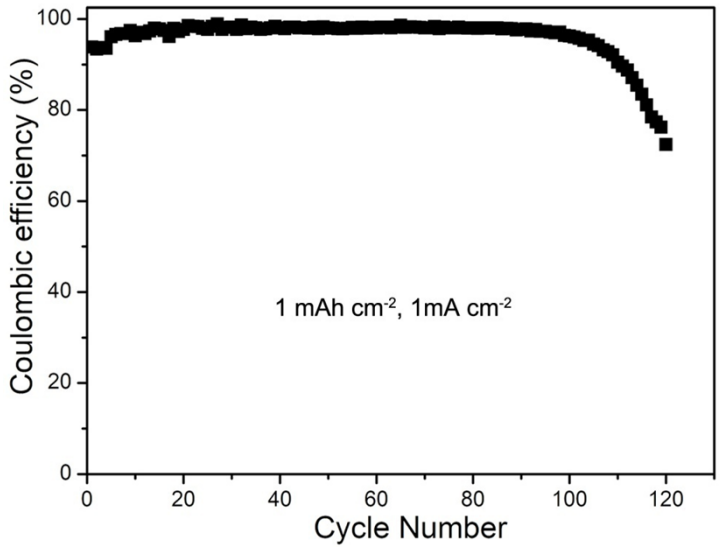

Fig. S17. The CE versus cycle number plot of the LMA on b-Cu using NaF as the electrolyte additive.

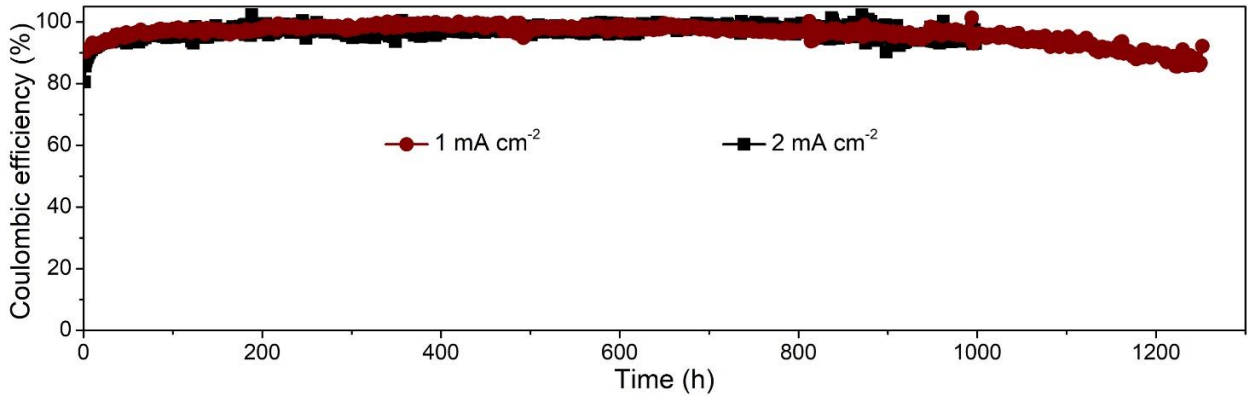

Fig. S18. The cycle life of the NMMF@C-Cu electrode at the current densities of 1 and 2 mA cm^{-2}.

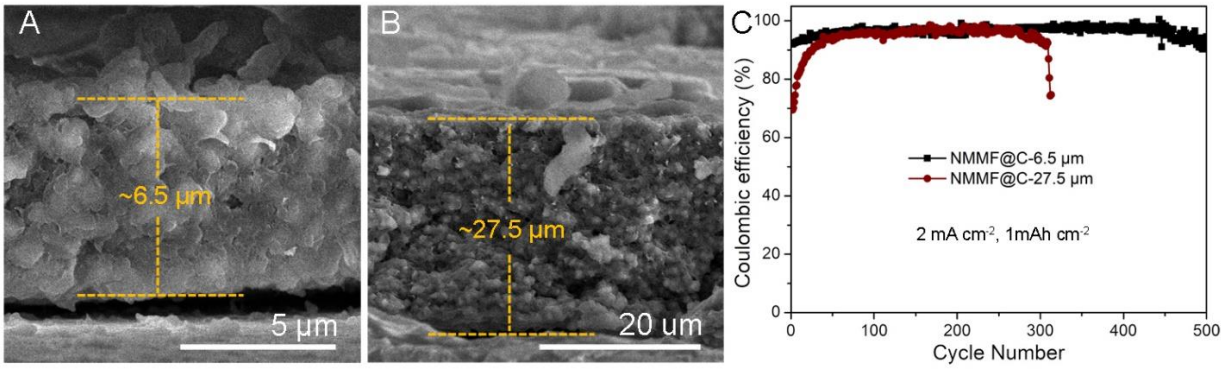

Fig. S19. Morphology and electrochemical performance of the Cu electrodes with different loading thickness of NMMF@C. (**A** and **B**) Cross-sectional FESEM images of the NMMF@C-Cu electrodes. (**C**) The CE of Li plating/stripping on NMMF@C-Cu electrodes.

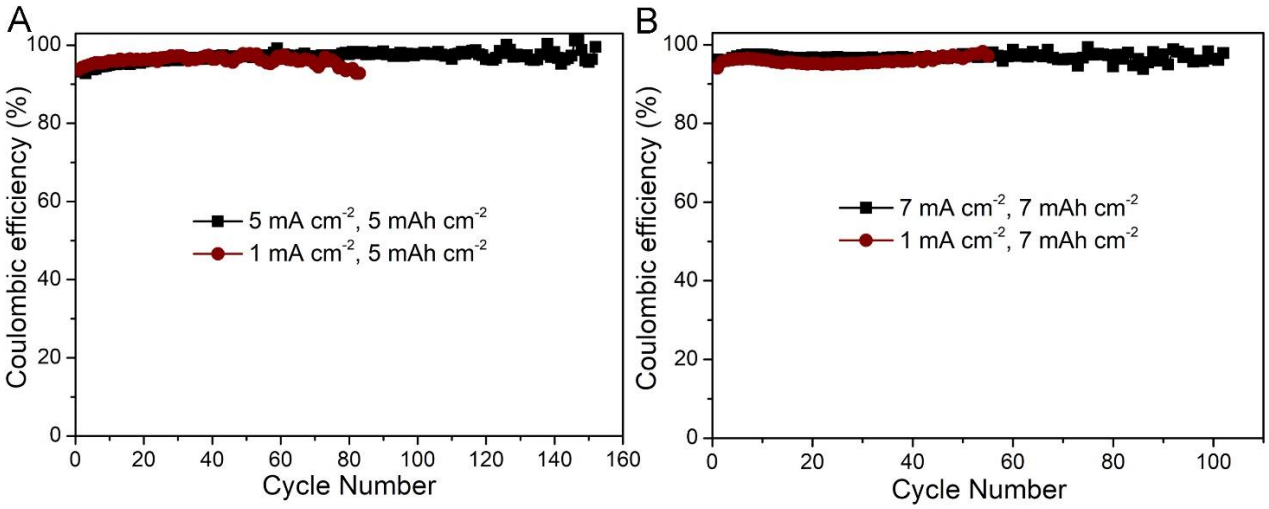

Fig. S20. The CE of Li deposition/stripping on the NMMF@C-Cu electrode at high areal capacities. (**A**) 5 mAh cm^{-2} and (**B**) 7 mAh cm^{-2}.

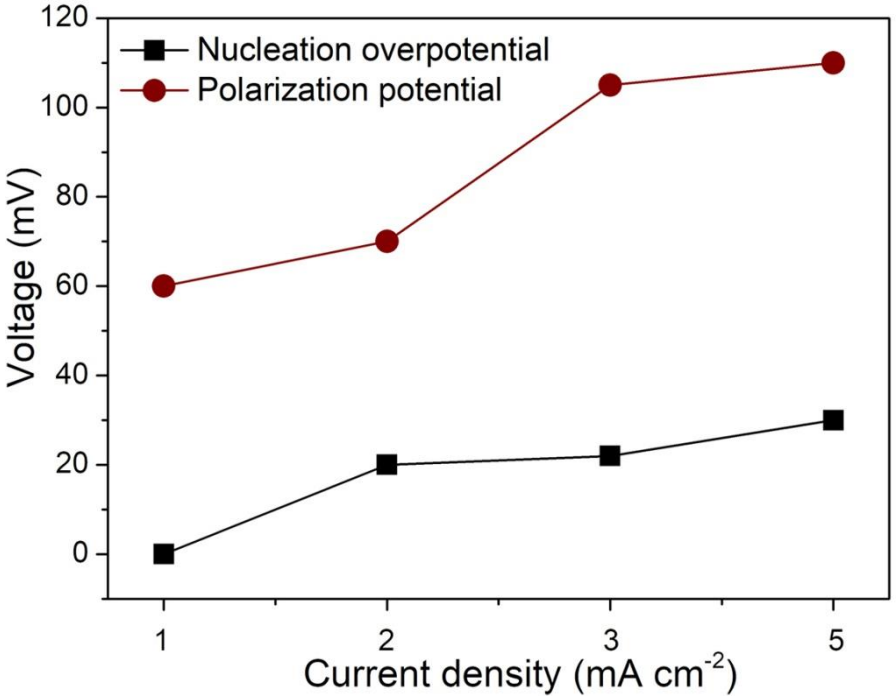

Fig. S21. Nucleation overpotential and polarization potential. The difference in nucleation overpotential and polarization potential of the NMMF@C-Cu anodes at different current densities.

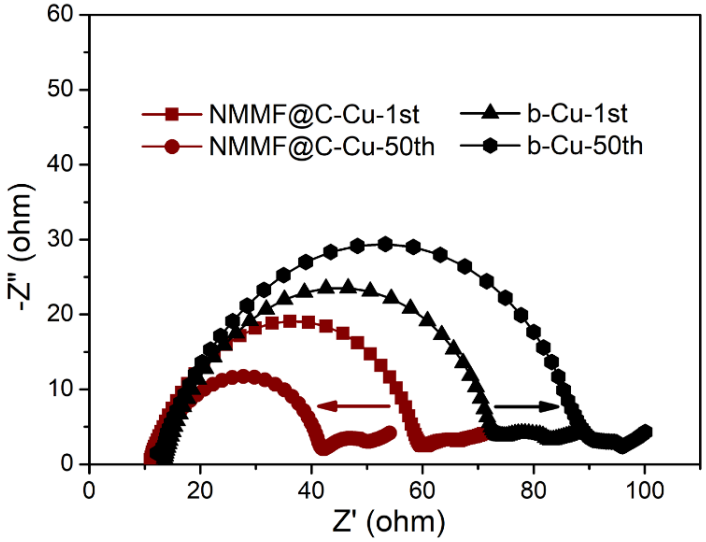

Fig. S22. The EIS plots of the NMMF@C-Cu and b-Cu electrodes after the 1st and 50th cycles.

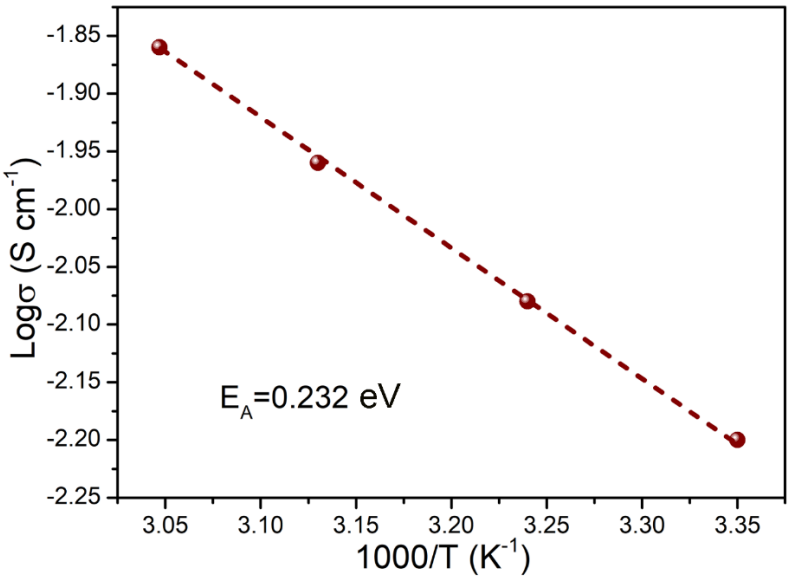

Fig. S23. Arrhenius plot of the symmetric NMMF@C-Li//NMMF@C-Li cell. The activation energy of the conductivity in the symmetric NMMF@C-Li//NMMF@C-Li cell was calculated from the slope of the Arrhenius plot. The activation energy of 0.232 eV indicates the high ionic mobility and diffusion in the symmetric cell.

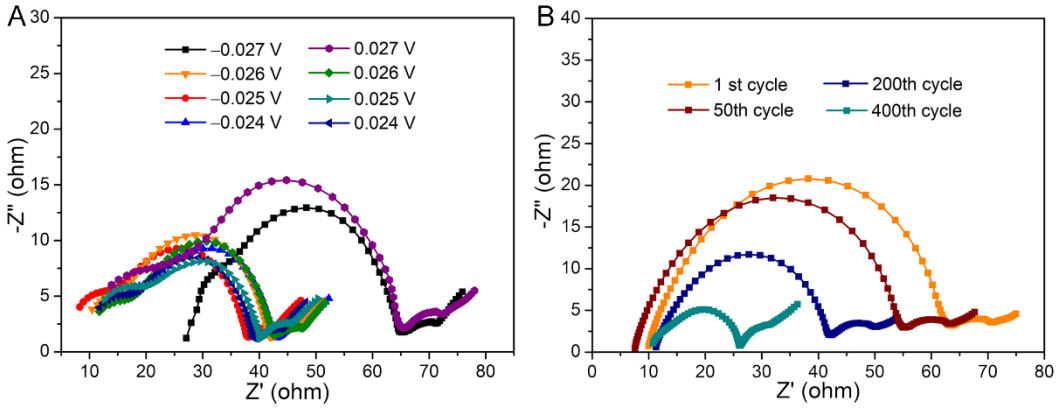

Fig. S24. EIS plots of the symmetric cell at 1 mA cm^{-2} for 1 mAh cm^{-2}. (**A**) EIS plots during the 10th cycle (**B**) EIS plots after the 1st, 50th, 200th, and 400th cycles.

The low impedance illustrated in fig. S24 demonstrates the good electronic conductivity in the symmetric cell. In addition, it is noted that the impedance of the symmetric cell decreases with the cycling, which may be attributed to the formation of stable SEI. More importantly, no inductive loops are found during the 10th cycle at different voltages and after the 1st, 50th, 200th, and 400th cycles, which indicates that no soft short occurred (*Electrochim Acta*. **223**, 85-91 (2017)).

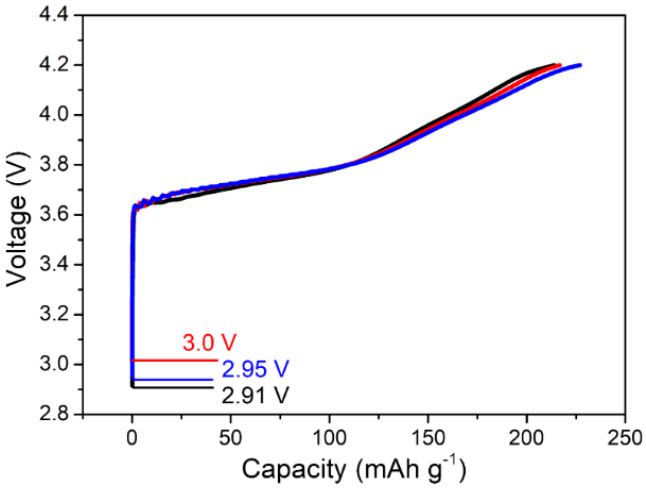

Fig. S25. The first charge curves of three NCM811/NMMF@C-Li full cells at the current density of 100 mA g^{-1}. From the first charge curves of full cells, the normal open-circuit voltage of around 2.95 V indicates that there is no electrical short circuit in full cells.

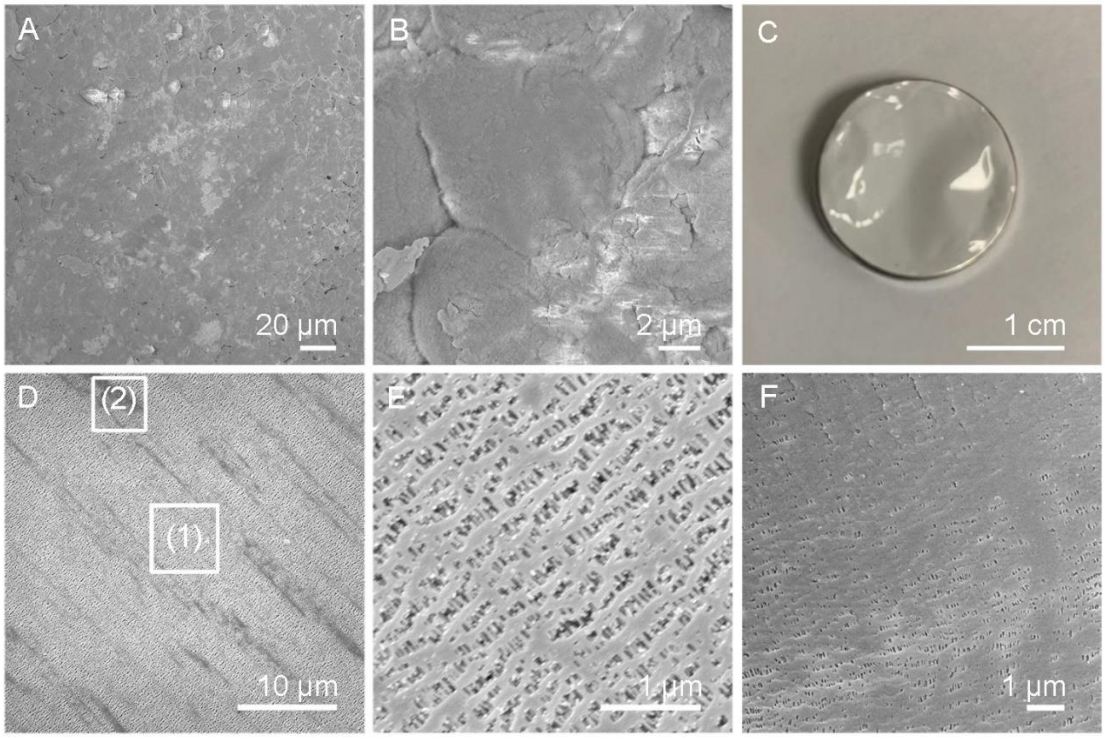

Fig. S26. FESEM images of the plated Li and separator in a symmetric cell after 400 cycles. (**A** and **B**) FESEM images of the NMMF@C-Li electrode in a symmetric cell after 400 cycles with different magnifications. (**C**) Optical image of the used separator in a symmetric cell after 400

cycles. (**D**) FESEM image of the used separator in a symmetric cell after 400 cycles. (**E**) Magnified FESEM image of the area (1) in fig. S26D. (**F**) Magnified FESEM image of the area (2) in fig. S26D.

As shown in fig. S26, A and B, the smooth surface of plated Li in the symmetric cell after 400 cycles indicates that there is no growth of Li dendrites in the symmetric cell. In addition, as seen from the optical and FESEM images of the used separator in the symmetric cell after 400 cycles (fig. S26, C-F), the integrity of the separator can also be observed. Therefore, there may be no soft short circuit existing in symmetric cells. Some holes are blocked in separator, which may be attributed to the formation of some organic composites from electrolyte.

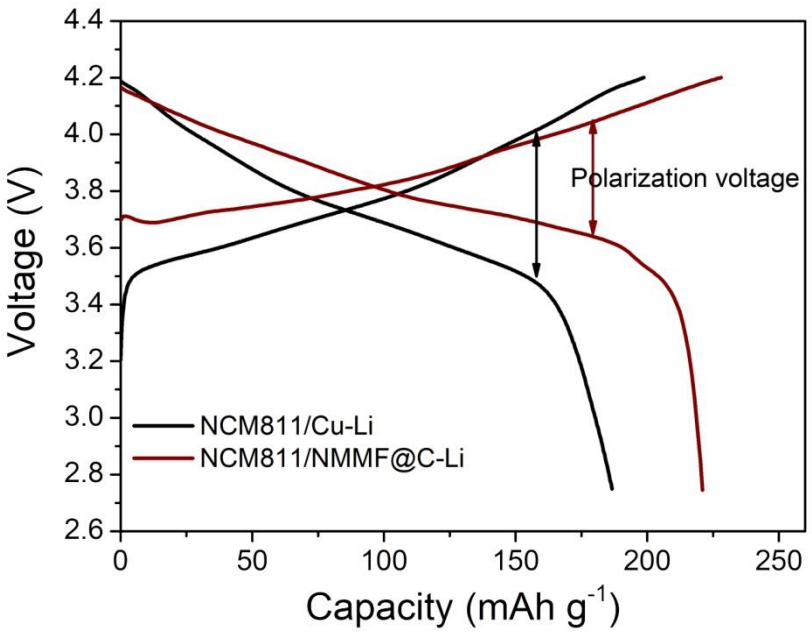

Fig. S27. Charge/discharge curves of full cells. The second discharge/charge curves of NCM811/Cu-Li and NCM811/NMMF@C-Li full cells.

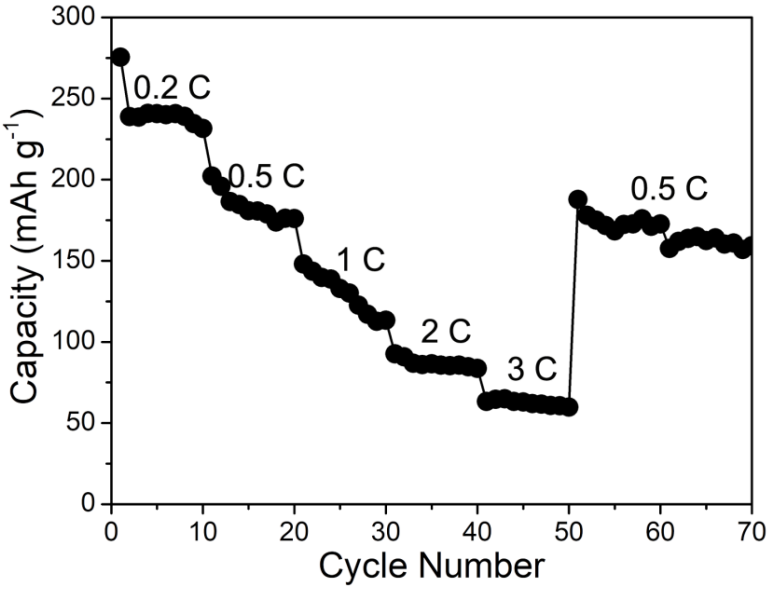

Fig. S28. Rate capability of the NCM811/Cu-Li full cell.

Table S1. The mass loss of NMMF@C in the ether electrolyte as a function of time.

Days (d)	2	4	6	8	10	12	14	16
Hours (h)	48	96	144	192	240	288	336	384
Mass of NMMF@C before soaking (mg)	39.57	39.46	39.71	40.43	39.44	39.59	39.87	40.59
Mass of NMMF@C after soaking (mg)	37.78	36.38	36.16	35.70	33.84	32.54	31.78	31.57
Mass loss ratio (wt%)	4.5	7.8	8.9	11.7	14.2	17.8	20.3	22.2

Table S2. The comparison of the CE of the anode in our work and some reported state-of-the-art anodes tested in the DOL/DME ether electrolyte.

Type of materials	Current density ($mA\ cm^{-2}$)	Capacity ($mAh\ cm^{-2}$)	Cycle number	Ref.
NMMF@C	**2**	**1**	**1000**	**this work**
NMMF@C	**1**	**1**	**600**	**this work**
3D porous poly-melamine-formalde-hyde	1	1	400	(*14*)
Coiled Cu wire	2	1	50	(*17*)
Polysulfides and $LiNO_3$	2	1	400	(*28*)
Polyimide with channels-coated stainless steel	2	0.5	150	(*30*)
ALD Al_2O_3/Hollow carbon spheres				
TiC/C	0.5	1	500	(*37*)
	1	1	100	(*48*)
α-Si_3N_4-membrane	2	1	100	(*53*)
Quaternized polyethylene terephthalate	2	1	100	(*54*)
Single-atom metals@N-doped graphene	2	1	150	(*55*)
3D porous Cu	2	1	125	(*56*)
3D glass fiber	2	0.5	60	(*57*)